Sustainable Marine Structures
https://journals.nasspublishing.com/index.php/sms

RESEARCH ARTICLE

Flow Structures around a Sphere Attached to the Bottom of a Prismatic Sloshing Tank: Problem-Oriented Basic Research

Murat Aksel [1*] , ***Oral Yagci*** [2], ***Manousos Valyrakis*** [3], ***V.S. Ozgur Kirca*** [4]

[1] *Department of Civil Engineering, Alanya Alaaddin Keykubat University, Alanya 07425, Antalya, Türkiye*
[2] *Civil Engineering Department, Engineering Faculty, Aydin Adnan Menderes University, Aydin 09010, Türkiye*
[3] *Department of Civil Engineering, Aristotle University of Thessaloniki, Thessaloniki 54645, Greece*
[4] *Civil Engineering Department, Istanbul Technical University, Istanbul 34555, Türkiye*

ABSTRACT

This study aimed to investigate the spatiotemporal variation of hydrodynamic variables around a sphere rigidly fixed to the bottom of a sloshing tank. The experimental measurement of the variations of dynamic variables around a body in a sloshing tank requires non-intrusive measurements that are usually expensive and sometimes inapplicable. Therefore, the numerical model could serve as a cost-effective tool for such problems. A two-stage analysis was conducted. In the first stage, an experimental study was carried out in a testing system comprising a water tank with uniaxial freedom of movement constructed on a monorail operated by a computer-controlled step motor. The primary objective of the experiments was to generate reliable data for calibrating the numerical model. During the experiments, the tank's movements were recorded using an accelerometer and ultrasonic sensors with a sampling frequency of 200 Hz for each. The accelerometer and ultrasonic sensor data were used to impose the motion of the sloshing tank into a Reynolds-Averaged Navier-Stokes (RANS)-based numerical model. The video recordings, which comprised temporal fluctuations of the water surface, were used to calibrate the Model 1. Once the first numerical model was calibrated based on water surface level records using image processing methods, the second numerical model was constructed to accommodate a rigid spherical body with a 17 mm diameter connected to the bottom of

*CORRESPONDING AUTHOR:
Murat Aksel, Department of Civil Engineering, Alanya Alaaddin Keykubat University, Alanya 07425, Antalya, Türkiye;
Email: murat.aksel@alanya.edu.tr

ARTICLE INFO
Received: 8 July 2024 | Revised: 9 August 2024 | Accepted: 15 September 2024 | Published Online: 22 September 2024
DOI: https://doi.org/10.36956/sms.v6i2.1204

CITATION
Aksel, M., Yagci, O., Valyrakis, M., et al., 2024. Flow Structures around a Sphere Attached to the Bottom of a Prismatic Sloshing Tank: Problem-Oriented Basic Research. Sustainable Marine Structures. 6(2): 42–63. DOI: https://doi.org/10.36956/sms.v6i2.1204

the sloshing tank. The initial and boundary conditions used in the second numerical model were identical to those used in the first model to measure the spatiotemporal fluctuations of the surrounding spherical body's kinematic and dynamic variables, respectively. The findings revealed that sloshing motion exerts a significant impact on the boundary layer separation process around the sphere. It was also witnessed that the stage of the sloshing motion controls the temporal lag between the pressure, velocity and water surface level.

Keywords: Boundary Layer Separation; Drag Force; Particle Hydrodynamics; Sediment Transport; Sloshing Tank; Oscillatory Flow; Wake Region

1. Introduction

1.1. Significance of Sloshing Problem for Industry

Sloshing, in its broadest sense, refers to the motion of a fluid with a free surface within a liquid container. Several fields, including maritime, ship transportation, aviation, space technology, building, equipment, and fuel storage, have investigated the phenomenon of sloshing within a confined volume [1–3]. Under certain conditions, some structures can contain rigid bodies at the bottom while experiencing sloshing. Significant sloshing-induced forces can be observed in both technological applications, e.g., offshore structures and marine vessels. Another example is baffled tank containers, which have baffles to reduce the impact of surges within the tank. Likewise, service reservoirs in a conventional water supply system may incorporate baffles for the same purpose. Another relevant local example is the residential complex known as One Rincon Hill in San Francisco. This skyscraper features a spacious water tank specifically intended to enhance its ability to withstand powerful winds and earthquakes. Other instances of these phenomena can be observed in nature and industry, such as waves and seiches occurring on the seabed or in lakes, as well as clarifiers, settling basins, and grit removal chambers.

1.2. Scope of the Study

In the implementations mentioned above, the focus was mostly on studying the interaction between fluid motion and complex objects, such as baffles in a sloshing tank. These studies were conducted as distinct case-specific problems. However, this study focused on a relatively simpler scenario, specifically the interaction between a sloshing tank and a spherical body. The main rationale for specifically targeting this case was to better understand the interaction between fluid motion in a sloshing tank and a sphere, i.e., acting as a basic obstacle. This investigation can contribute foundational knowledge to various fields, such as marine, coastal, and structural engineering. Moreover, the outcomes of this study may provide a useful perspective in interpreting more complex cases in the industry. Although the flow-sphere interaction under steady flow conditions has been widely examined in the pertinent literature, the flow around the sphere under sloshing still needs to be better understood due to the complex spatiotemporal flow field fluctuations around the body.

The drag force acting on a body undergoing unsteady flow differs from that in a steady flow, with the primary difference being the fluctuation of the force [4, 5]. Vortex shedding is a prominent feature of unstable flow around a sphere. As the flow fluctuates, the sphere's surface sheds alternating vortices. Vortices are created in the area behind the sphere, called the wake region. These vortices can cause flow instability and pressure fluctuations. During each oscillation cycle, the wake changes between different patterns. The interaction of the vortices with the oscillating flow field plays a dramatic role in the overall flow dynamics. Considering this vision, our objective has been to gain a deeper understanding of the occurrence of the wake region and the forces that form depending on the stage of the sloshing motion.

1.3. Earlier Studies

When the direction and magnitude of fluid acceleration change considerably, as they typically do in sloshing tanks, the resulting delay in boundary layer development cannot be ignored. Odar and Hamilton[6] experimented with oscillating flow across a sphere to improve Bassett's solution. Anderson and Uhlherr[7] experimentally investigated the influence of turbulence intensity on the drag coefficient of freely entrained spherical particles in fully developed pipe turbulence when the Reynolds number was between 200 and 2000. According to their findings, the mean particle drag coefficient increases by 20% relative to the empirical drag law at turbulence intensities of 0.1–0.2 but does not change noticeably at turbulence intensities of 0.25–0.35. Later, Mei[8] provided a generic dynamic equation that included quasi-steady drag, history force, and added-mass force in the time domain for particle movements with a finite Reynolds number (order of several hundred). Using a numerical computation approach, Chang and Maxey[9] studied the oscillating flow over a sphere at frequencies up to 10 Hz and Reynolds numbers up to 16.7. They employed numerical modelling to examine a fluctuating flow past a sphere at a low Reynolds number (Rep < 20). Their research showed that separation occurred during the deceleration phase but not during the acceleration period, which held even at extremely low Reynolds numbers. At this Reynolds number, flow separation has been reported for a fluctuating flow over a sphere, which was not detected for a steady flow. However, it is important to note that this particle's Reynolds number value is lower than those examined in prior studies. The outcome of a numerical analysis done by Alassar and Badr[10] on the flow field and forces of a spherical particle in a fluctuating freestream flow revealed a temporal lag between the unsteady drag and the freestream flow.

As previously indicated by Song and Graf[11], hysteresis effects between physical variables are inevitable when there is a temporal lag between the occurrence moment of water's surface and the dynamic quantities acting on the obstruction. The experimental findings of Gargari et al.[4] and Erdog et al.[5] showed that the role of hysterical effects around a solid structure under unsteady flow should be addressed at the design stage. Brucato et al.[12] experimentally determined a particle's mean drag coefficient in a turbulent flow. According to their findings, the influence of turbulence fluctuation on particle drag depends on particle size and intensity. Turbulence fluctuation may dramatically increase drag if the particle size is large, whereas it has minimal influence on drag if it is small. Luo et al.[13] investigated the response of force behaviours of a fixed spherical particle undergoing a fluctuating freestream flow using the immersed boundary approach. Data from their research showed that the mean drag is at its highest when the flow frequency equals the natural vortex shedding frequency. Later, Valyrakis et al.[14, 15] examined and modelled[16] the effects of turbulent fluctuations around small spherical bodies in rough boundary sheared flows and how they affect particle dynamics.

The hydrodynamic quantities observed in the sloshing tank are a consequence of the container qualities (i.e., width, length, initial water depth, shape, surface roughness), external force characteristics (e.g., wave, seiche, earthquake, inertial forces), and fluid properties (dynamic viscosity, density, surface tension). Depending on the type of agitation and container form, the free liquid surface can undergo a variety of motions. These can vary from simple planar to non-planar, spinning, irregular beating, symmetric, asymmetric, quasiperiodic, or chaotic motions. While some variables may become the primary determinants, others may only play a minor role in the motion. Which variable will become prominent is greatly determined by the ratios between the motion frequency and the structure's natural frequency.

A two-dimensional examination of liquid motion in rectangular tanks reveals that the liquid depth-to-width ratio is a significant driver of the natural frequency. Depending on the depth of the liquid within, rectangular tanks may exhibit one of two unique forms of sloshing behaviour. High liquid fill depth is defined as a ratio of liquid depth to the tank's cross-sectional width along the direction of motion greater than 0.2[17]. There have been reports of hydraulic jumps and travelling waves in shallow sloshing during excitation periods around resonance[2, 3].

When a sphere resting on top of a solid boundary experiences a periodic flow domain like a sloshing tank, the resulting coherent flow structures advected past the spherical body have distinct features. The interplay between the flow and sphere is profoundly influenced by the characteristic nondimensional parameters, such as the particle Reynolds number, defined by flow (such as the approach flow velocity), object (specifically the diameter of the sphere), and fluid (i.e., density, viscosity) features. The flow pattern created in the wake zone significantly impacts the forces acting on the sphere (i.e., form drag and skin friction). Therefore, resolving the flow pattern around the spherical body yields practical insights.

1.4. Governing Forces

In a sloshing tank, the sphere, which is firmly attached to the bottom for this experiment, is primarily subjected to in-line forces. In this case, the gravitational, lifting, buoyancy, and Magnus forces can be disregarded as the sphere is rigidly attached to the bottom. In this case, the total force acting on the sphere is only in the in-line direction and is given by Equation (1). The first term on the right-hand side of Equation (1) represents the "drag force" (commonly denoted by F_D), which is the in-line force acting upon the sphere. Drag force directly results from the pressure and shear distribution acting on its surface[18]. The resulting drag is directly influenced by the boundary layer flow characteristics[19], which are largely controlled by the Reynolds number[20, 21], turbulence[22, 23], the form of the object[22, 24, 25], the degree of flow/wave unsteadiness[4, 5], and the arrangement of the obstacle if the body consists of multiple obstacles[26, 27]. The multiplication of U|U| in the drag force expression ensures that drag is always in the direction of velocity. The second term is the hydrodynamic mass (also known as added mass), which is defined as the mass of the fluid immediately surrounding the sphere that is accelerated because of the sphere's presence during the fluid motion and is influenced by the pressure on it (Sumer and Fredsøe[20], p. 130). Finally, the last term is known as the Froude-Krylov force, which originated from the accelerated motion of the fluids in the outer flow region[20]. This acceleration in flow in the outer region would generate a pressure gradient (or vice versa) as defined in Equation (3). It should be noted that if the otherwise stationary sphere moves with the fluid motions, no pressure gradient will be caused by the acceleration of the surrounding flow. As a result, the Froude-Krylov force will not be present in this scenario.

$$F = \frac{1}{2}\rho C_D A U\left|U\right| + m_f C_m \dot{U} + m_f \dot{U} \tag{1}$$

in which F = total in-line force, ρ = fluid density, C_D =drag coefficient, A = projected area of the sphere which is equal to $A = \pi D^2/4$ (D is the diameter of the sphere), U=fluid velocity, m_f = the mass of the fluid that is influenced by the presence of the sphere and experiences acceleration during fluid motion (equal to $\rho_f \forall_f$, where $\forall$ is the volume of the fluid displaced due to sphere) $C_m =$ hydrodynamic mass coefficient (added mass coefficient) which is equal to 0.5 for sphere[20], $\dot{U}$ is the acceleration of the flow in the outer region. It emerges as the result of the spatial pressure gradient.

$$\dot{U} = \frac{dU}{dt} \tag{2}$$

$$\frac{\partial P}{\partial X} = -\rho\frac{\partial U}{\partial t} \tag{3}$$

in which P = pressure value at the far field, X=in-line distance between consecutive points where pressure values are recorded/considered. It should also be noted that for a spherical body, the multiplication of "$m_f\dot{U}$", which is a common term in the expressions of hydrodynamic mass and Froude-Krylov force, can be re-written as below:

$$m_f\dot{U} = \rho\left(\frac{\pi D^3}{6}\right)\dot{U} \tag{4}$$

Based on the definitions of the above influential variables, the total in-line force acting on a cylinder in a water environment with acceleration, where the sphere remains stationary, may be expressed below.

$$F = \frac{1}{2}\rho C_D A U\left|U\right| + m_f\dot{U}(C_m + 1) \tag{5}$$

The summation term of $(C_m + 1)$ can be expressed under a new coefficient C_M. The term $m_f\dot{U}(C_m + 1)$ is called inertia force.

$$F = \frac{1}{2}\rho C_D A U\left|U\right| + m_f C_M \dot{U} \tag{6}$$

1.5. Objective of the Study

Considering the arguments presented above, the primary aim of this study was to analyse the flow field around a sphere attached at the bottom of a tank subjected to a unidirectional and periodic excitation. An experiment was conducted in a prismatic sloshing tank. The experimental data was employed to calibrate and validate a three-dimensional numerical model. The objective was to utilise the numerical model to gain insight into the flow structure around the spherical body. In addition, the following research questions, which may be of relevance to the implementation of the project in practice, were also investigated:

- Can we effectively utilize a RANS model to understand the sensitivity of vortices generated by flow conditions as the flow oscillates in a sloshing tank?
- How do hydrodynamic variables vary around a spherical body fixed rigidly to the bottom of a sloshing tank?
- During sloshing, how does the shear stress in the neighbourhood of the sphere change?
- How do the dynamic and total pressures around the spherical object during the sloshing change?

2. Method, and Limitations

The interaction between oscillatory flow and sphere is a complex hydrodynamic phenomenon. A series of laboratory experiments were conducted to investigate this problem. In the experiments, the bidirectional flow was generated inside a rectangular sloshing tank in case no sphere was present. The results from the laboratory experiments were used to calibrate the numerical model. Once the numerical model was calibrated, a rigid/spherical object was incorporated into it.

As discussed in Section 5.1, three modes of sloshing motion were described in this study to facilitate the flow analysis. For the numerical study, which accommodates a sphere rigidly fixed to the solid boundary of the tank, certain assumptions and idealisations were adopted for simplicity and to match the physical model best. These are as follows:

(1) The bed of the tank was rigid, horizontal, and hydraulically smooth (i.e., clean glass, as done in the physical experiment),

(2) The sphere was kept at a fixed position (located at the centreline of the tank),

(3) The object was perfectly spherical.

3. Experimental Setup and Measurement Techniques

3.1. Flume and Measurement Devices

Experimental studies were carried out in the hydraulics laboratory of the Civil Engineering Department of Alanya University. The sloshing tank is 28 cm in length, 10 cm in width, and 5 cm deep. A small tank size was intentionally chosen to minimise the errors occurring during the digitisation of the video recordings that would later be used to calibrate the numerical model. The sphere diameter was 17 mm, and the water depth in still condition was 50 mm. The ratio of the sphere's diameter to the depth of the still water was maintained at a constant value of 0.34 throughout the experiments. To facilitate the visualisation of flow movement, red food dye colouring was added to the water before each experiment. The testing system consists of a water tank with uniaxial freedom of movement, built on a monorail driven by a computer-controlled step motor. Care was taken to ensure the experiments were conducted under identical controlled conditions. Specifically, room temperature and humidity were kept constant throughout the tests at 22 °C and 55%, respectively. An accelerometer and ultrasonic sensor were applied concurrently to record the motion of the shaking table. The accelerometer, capable of recording data at 100 Hz, was mounted on a shaking table. During the tank's motion, the ultrasonic sensor measured the distance between the sensor and the tank's left sidewall. Additionally, a video camera, which was attached to the shaking table, was used to capture the temporal variation of the water surface in the tank (**Figure 1**).

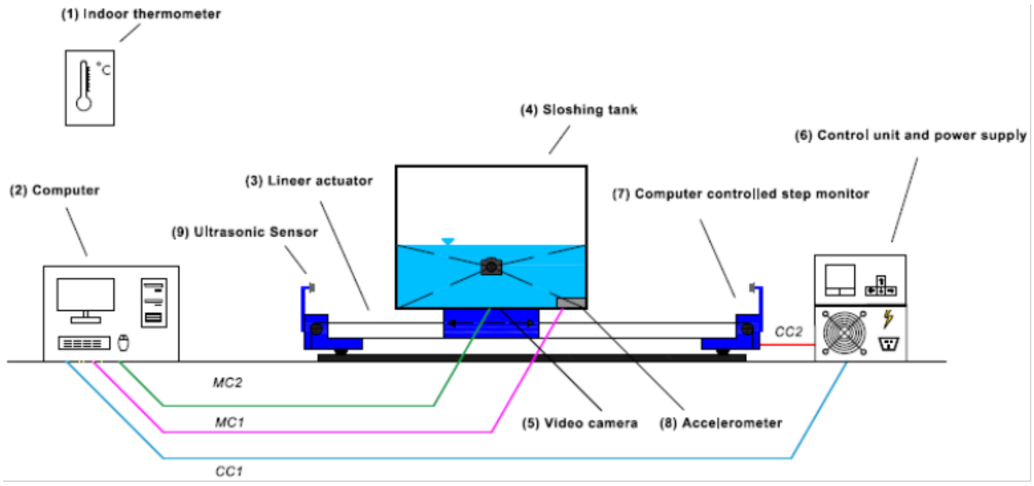

Figure 1. Schematic of the experimental Setup, (l) indoor thermometer, (2) computer, (3) linear actuator, (4) tank, (5) video camera, (6) Control unit and power supply, (7) step type computer-controlled motor, (8) accelerometer. Green and red lines show control cables 1 and 2 (CCI), (CC2), and magenta and light blue coloured lines present monitoring cables (MC l), (MC2), respectively.

3.2. Quantification of Tank and Fluid Motions

During the experiments, the tank's motion was controlled by signals produced in the computer domain with T = 2.81-second periods. Once the tank's motion commenced, data collection by the video camera, ultrasonic sensor, and accelerometer was synchronously initiated. The video camera collected data with a 60-fps frame rate and 1080-pixel resolution. Video records obtained during the sloshing were processed using MATLAB image processing tools.

The objective of utilising this image processing technique was to quantify the surface variation of the water during sloshing. Based on these records, temporal variations of water surface level at certain characteristic points spanning the dimension of the physical model in the flow-wise direction were obtained. As detailed below, the acquired water surface elevations were utilised to calibrate the numerical model. The ultrasonic sensor measured the instantaneous distance between the probe and the left wall of the sloshing tank. The accelerometer quantified the instantaneous acceleration of the sloshing tank as well. The objective of measuring the movement of the sloshing tank using both an accelerometer and an ultrasonic sensor was to validate the results obtained and to ensure the use of a credible dataset for the numerical model. This serves to increase the reliability and quality of the model-generated data. During the records sampling frequency, the ultrasonic sensor and the accelerometer were 200 Hz.

3.3. Data Processing

During experiments, once the sloshing tank was set in motion, the video camera, accelerometer, and ultrasonic sensor collected data synchronously, i.e., their initial moments in the time domain were identical. This method enabled processing datasets that shared a common temporal beginning in a more streamlined fashion. The video recorded with a 60-fps frame rate was decomposed into individual frames. Afterwards, a masking process was applied to each frame (**Figure 2**) following their pixel content (i.e., Red-Green-Blue, RGB values). The unmasked pixel numbers were quantified for the tank's left side to estimate the sloshing wave height. Recorded accelerometer data was processed utilising the code Seismosignal, an efficient and widely used software by earthquake engineers in baseline correction/conversion. The despiking of the displacement data, which were acquired by both accelerometer and ultrasonic sensor, were processed in Matlab as shown in **Figure 3**.

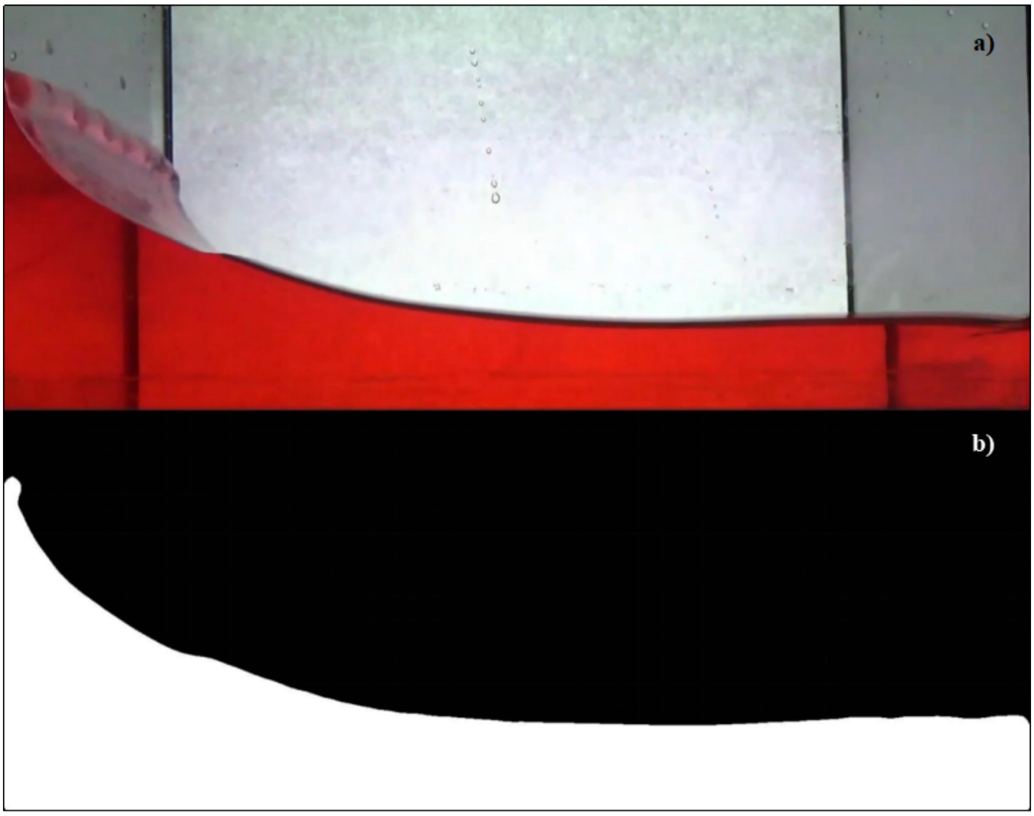

Figure 2. Demonstration of the applied masking process and image processing procedure for the identification of the free water surface within the sloshing tank: **a**) importing raw image, **b**) converted into black and white.

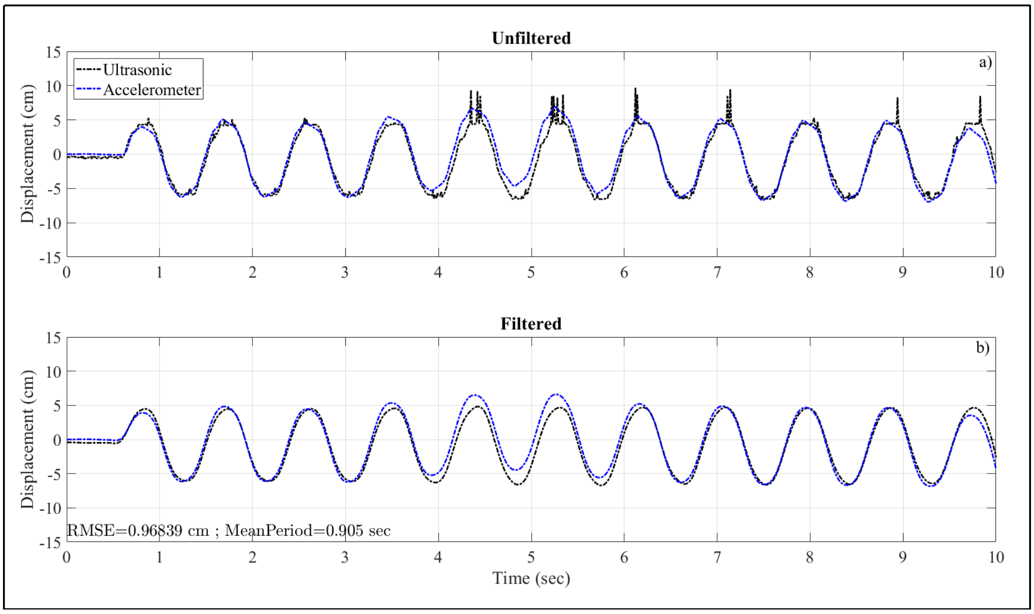

Figure 3. Recorded time series of the tank displacement using ultrasonic distance sensor (black dashed line) and recording from the accelerometer mounted on the shake-table (blue dashed line), **a**) is unfiltered data and **b**) is filtered data using robust quadratic regression filter in MATLAB. Mean period of the tank motion and root mean square error of the accelerometer results to ultrasonic sensor results are presented at the left downside of each graph on the right column.

4. Numerical Model and Validation

4.1. Methodology for the Numerical Studies

Measuring certain physical variables, such as velocity, turbulence, and bed shear stress, around a spherical body in a sloshing tank may be costly and sometimes even technically inapplicable. Hence, numerical models enable us to investigate the problem in-depth and emerge as a cost-effective tool. Therefore, a two-staged analysis was conducted during the numerical modelling study.

- Firstly, a model was developed that particularly aimed to simulate the variation of water surface in the sloshing tank with acceptable accuracy. The primary concept behind this model, which does not account for the presence of the spherical body in the sloshing tank, was to prepare a flow domain as a background for the examined problem (i.e., flow around the spherical body in the sloshing tank). Once the background numerical model was calibrated based on video (used for verifying water surface variation in the tank) and displacement records (used for representing the water surface motion in the numerical domain), this is followed in the second stage of the numerical model.
- In the second phase of the model, the spherical body in the sloshing tank was placed into the centre of the bottom of the calibrated numerical model. Based on this numerical model, the temporal variation of certain fundamental dynamic variables around the spherical body was obtained. The flow chart summarising the above processes is depicted in **Figure 4**.

4.2. Model Specifications

Computational Fluid Dynamics (CFD) based sloshing analysis was performed using Reynolds Averaged Navier-Stokes (RANS) equations with the help of Flow-3D software, which is commonly used in various disciplines[28–35]. In addition, this solver is also used in sloshing analyses with confirmation by experimental studies and calculates results compatible with the experimental results[1, 36, 37].

The continuity equation expresses the conservation of mass. For a given flow domain, it can be given as Equation (7).

$$\frac{\partial \rho}{\partial t} + \nabla .\left(\rho \boldsymbol{u}\right) = 0 \tag{7}$$

In here, ρ is the fluid density, $\boldsymbol{u}$ is the velocity vector and t indicate time. In incompressible flow, the density ρ is constant, and the continuity equation simplifies to the condition that the divergence of the velocity field is zero.

The momentum equation is derived from Newton's second law and is used to describe the motion of fluids. It can be expressed as Equation (8).

$$\frac{\partial\left(\rho \boldsymbol{u}\right)}{\partial t} + \nabla .\left(\rho \boldsymbol{u}\boldsymbol{u}\right) = -\nabla p + \nabla . \tau + \rho \mathbf{g} + \boldsymbol{F}_{ext} \tag{8}$$

In Equation (8), p is the pressure, τ is the viscous stress tensor, g is the gravitational acceleration and F$_{ext}$ represents external forces. The viscous stress tensor, τ is given in Equation (9).

$$\tau = \mu\left(\left(\nabla \boldsymbol{u} + \left(\nabla \boldsymbol{u}\right)^{T}\right) - \frac{2}{3}\left(\nabla . \boldsymbol{u}\right)\boldsymbol{I}\right) \tag{9}$$

In here, μ is the dynamic viscosity and *I* is the identity matrix.

4.3. Validation and Calibration

As stated above, the experimental data, which aims to simulate the temporal variation of the water surface during sloshing, underpinned background data for the validation and calibration of the first numerical model. The video records showing the water surface variation during sloshing were used to calibrate the first model. **Figure 5** shows the water surface elevations observed based on the experiments, and the numerical model was given for a direct comparison. In addition to this visual-based assessment, a similar comparison was also made in a quantified manner (**Figure 6**). As can be inferred from **Figures 5** and **6**, Model 1, which serves as Model

2's benchmark, simulates the change in water surface elevation in the sloshing tank with acceptable accuracy. As shown in **Figure 4**, once the first numerical model was calibrated, the same model was equipped with a sphere. To ensure that the obtained numerical outcomes are independent of the mesh resolution, mesh sensitivity/independence analysis was undertaken after the calibration of the model. The tests revealed that the produced numerical outputs were independent of the imposed mesh conditions.

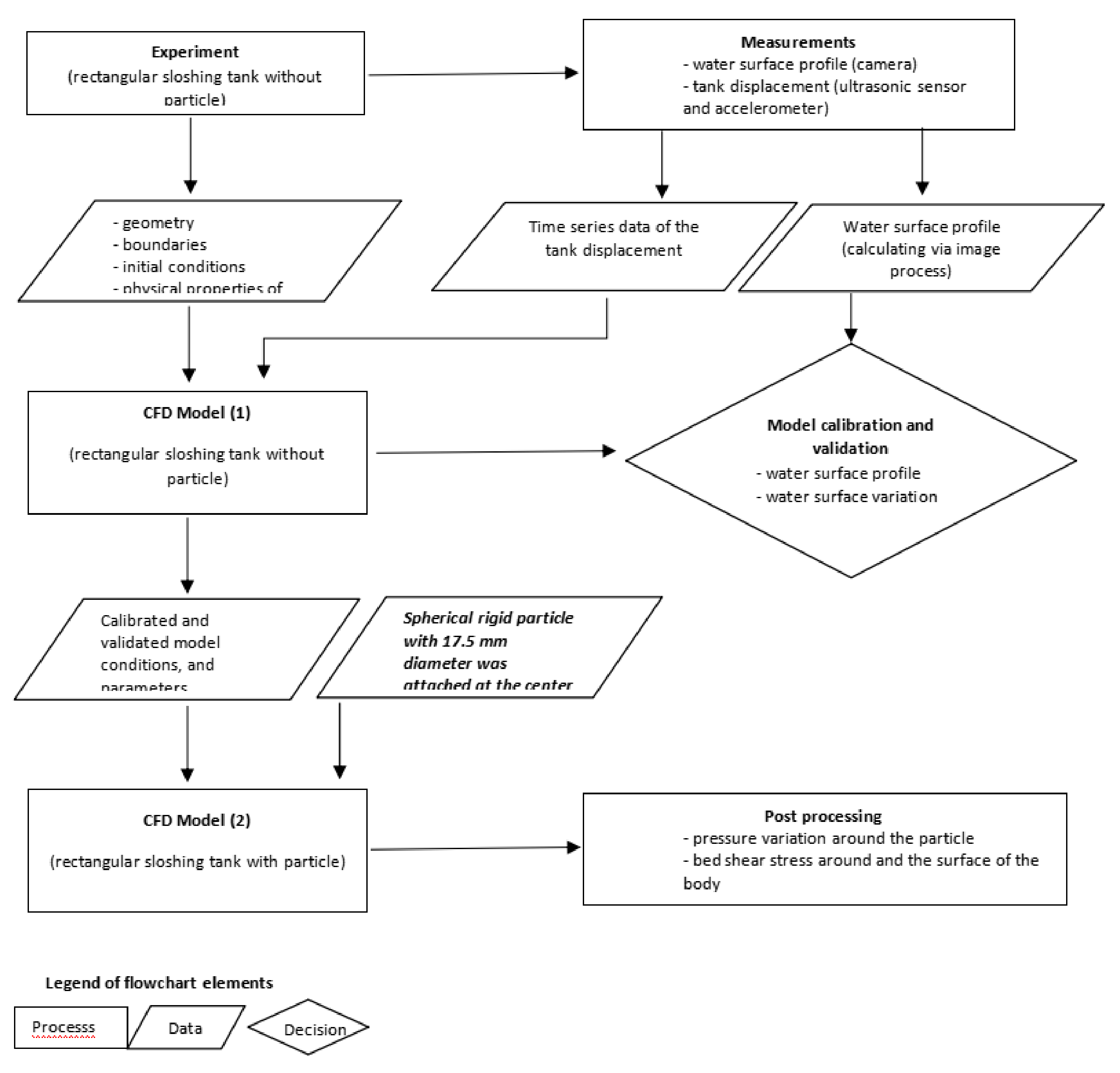

Figure 4. A flow chart showing how the experimental data are implemented for setting up the CFD model and calibrating it.

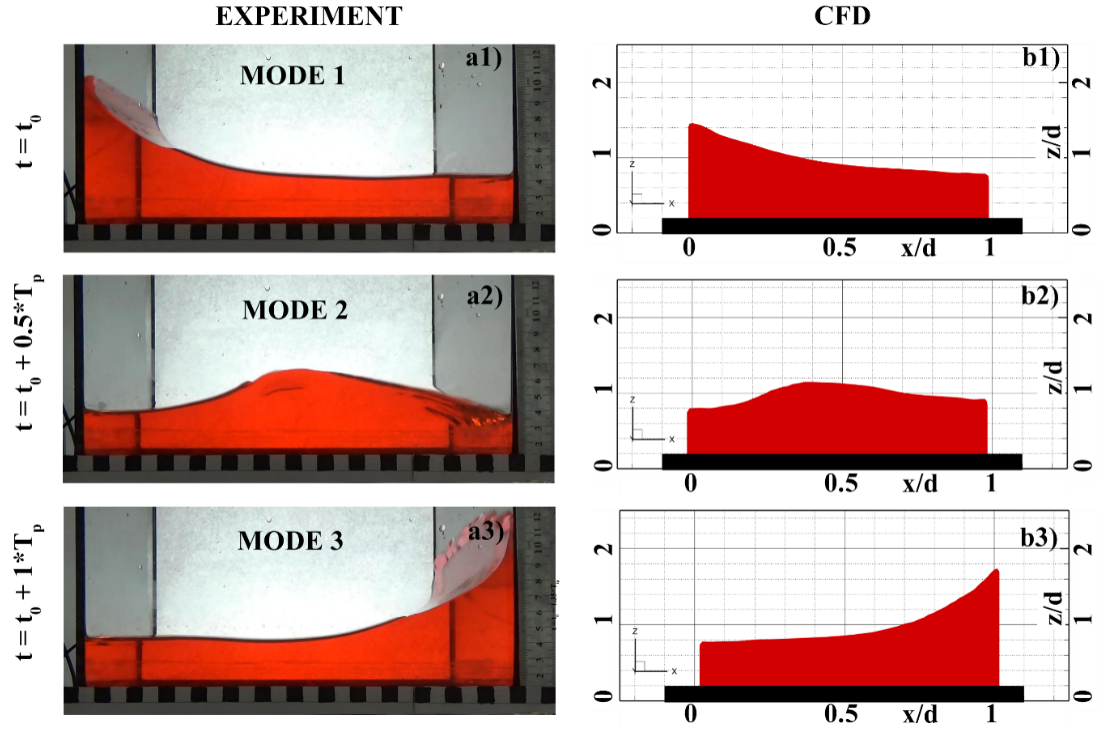

Figure 5. Demonstration of the visual verification of the computational model outputs for the typically observed modes. **a1–a3**) the pictures captured from the video and **b1–b3**) CFD model results for the water phase. The dimension of the ruler adjacent to sub-figures "a" is in cm. The squares located at the bottom of each sub-figures "a" are 1 cm x 1cm. The period of the cyclic motion of sloshing tank was 0.905 seconds. The complete video record can be accessed via supplementary material links given at the end of this study.

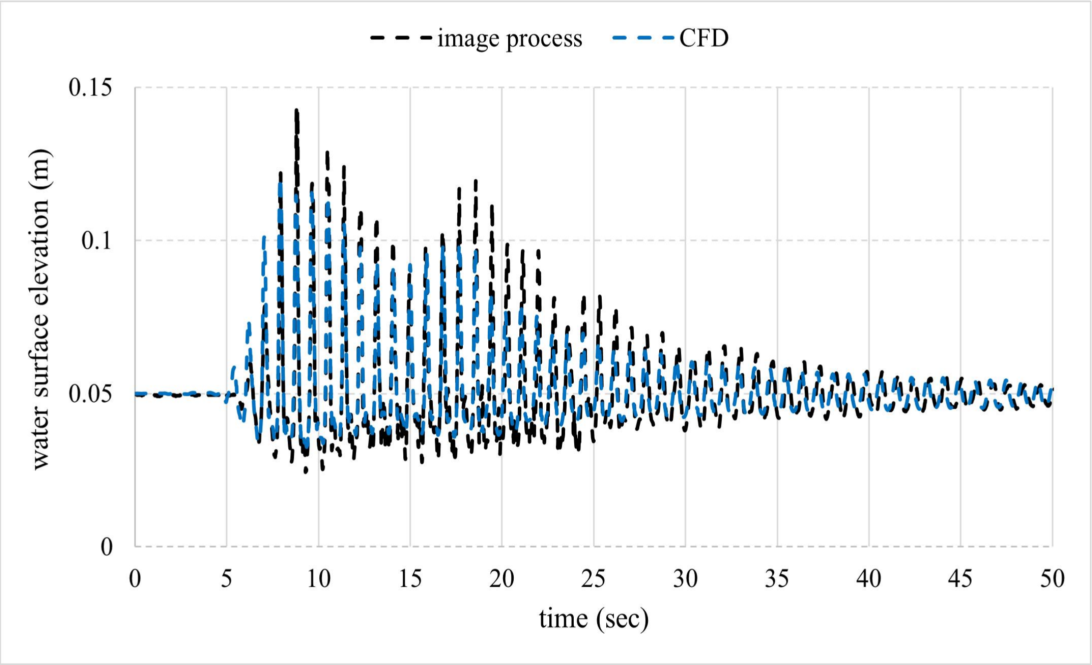

Figure 6. Recorded and modelled time series of the water surface elevation at the left-hand side of the tank during the test 1 was calculated via image process and CFD. Image process and CFD results were presented with black and blue lines, respectively.

5. Analysis of the Results

Based on numerical model 2, the spatiotemporal variations of physical variables were analysed for the cyclic motions of the sloshing tank. While some of the results were presented here for one whole cycle period of the sloshing tank, which is equal to 0.905 seconds, some of the results were analysed for the half-cycle period of the sloshing tank. The period of motion is described as the duration required for the cyclic motion of the tank from right to left and left to right. In this section, the modes of the sloshing motions were described. Secondly, the velocity and vorticity domains with/without sphere cases were given comparatively for the different modes. Lastly, the spatio-temporal variations of hydrodynamics variables around the spherical body within the tank were investigated.

5.1. Definitions of Three Basic Modes of Sloshing

The sloshing motion was conceptually discretised into three major modes **(Figure 7(a1–a3))**. The classification was devised with the intention of facilitating the analysis and interpretation of the results. This classification was based on the conception that during the sloshing motion, the influential forces change from one to another at specific characteristic moments. A description of these three major modes is provided below.

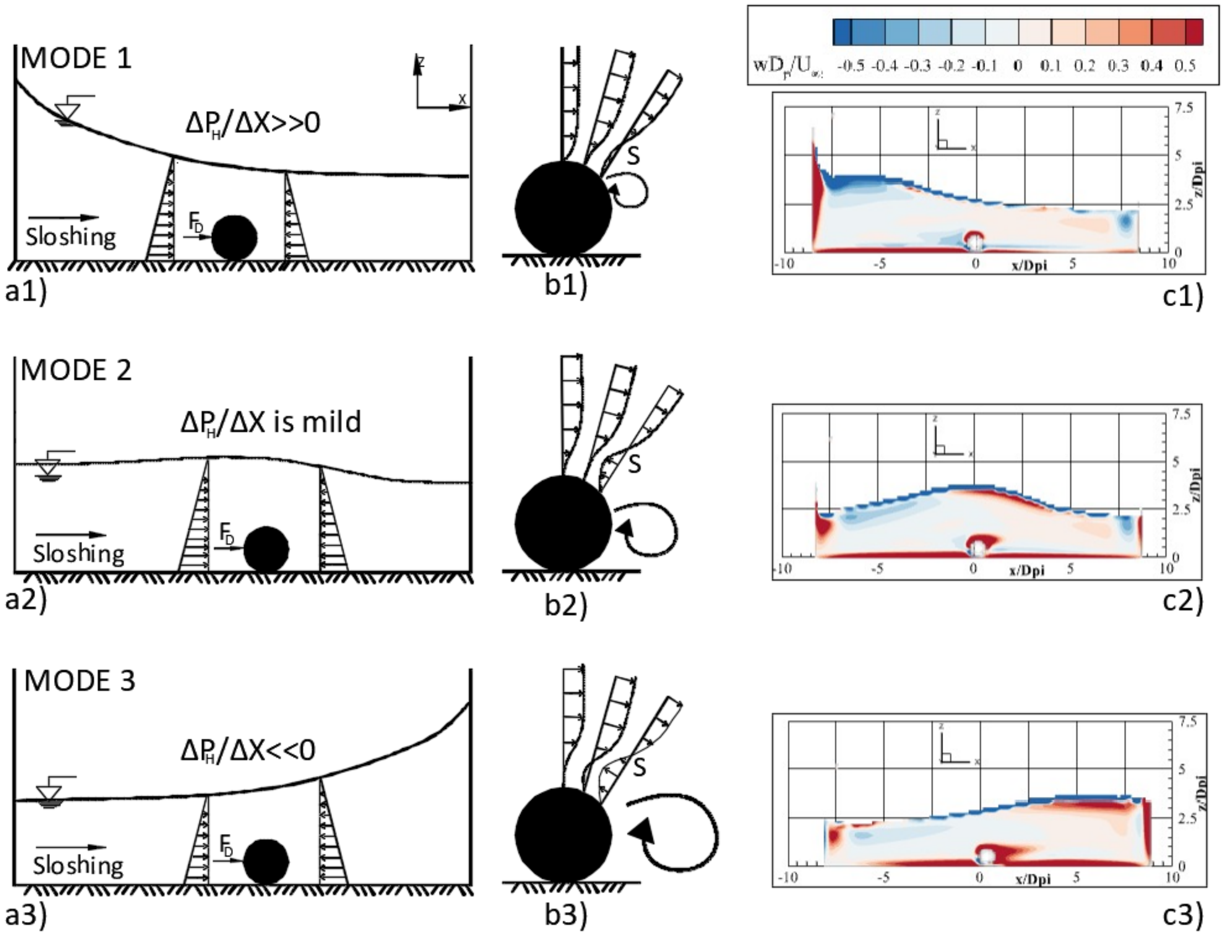

Figure 7. Three modes of the sloshing during half cycle period (**a1–a3**), conceptual figures which show the shifting of boundary layer separation point towards upstream due to decreasing hydrostatic pressure gradient (**b1–b3**), corresponding non-dimensional vorticity fields calculated by the numerical model (**c1–c3** extracted from **Figure 7**).

Mode 1: In this mode, the instantaneous net hydrostatic pressure gradient due to far-field pressure gradient, i.e., Froude-Krylov Force is maximum (∂P/∂X in Equation (3)). This force and drag force (FD) are in the same direction at the beginning of the half-sloshing cycle.

Mode 2: The moment the sloshing wave passes over the spherical object. In this mode, the far field hydrostatic pressure gradient is minimal due to the mild slope of the water surface, i.e., ∂P/∂X, and drag force (F_D) is maximum due to enhanced velocity near the sphere. The directions of these two force components are still the same.

Mode 3: As in Mode 1, the net far field hydrostatic pressure gradient, ∂P/∂X, i.e., the Froude-Krylov force, is maximum. This force and drag force (F_D) are in opposite directions.

MODE 1:
The direction of the net hydrostatic pressure gradient is in the same with flow induced drag force
Low velocity field around the sphere (see **Figure 8(b1,b2)** for the relevant velocity profiles)
The net hydrostatic pressure gradient pushes the separation point of "S" towards downstream is high
RESULT: Retardance in separation and weaker vorticity rear the sphere

MODE 2:
Wave crest passes over the spherical body
Highest velocity field around the sphere (see **Figure 8(c1,c2)** for the velocity profiles)
Drop in net hydrostatic pressure gradient which pushes separation point of "S" towards downstream.
RESULT: Earlier boundary layer separation and enhanced vorticity in the wake region of sphere

MODE 3:
The direction of the net hydrostatic pressure gradient is opposite to the flow induced drag force direction.
High velocity field around the sphere (see **Figure 8(d1,d2)** for the velocity profiles)
Opposite direction in pronounced net hydrostatic force pushes the separation point towards upstream
RESULT: Earliest boundary layer separation and the occurrence of most distinct vorticity

It should be noted that, although not shown here, the same conceptual figure could be produced for the opposite direction of the sloshing motion (i.e., for the mass transport direction from right to left). To better describe the modes, the contour plots showing the variation of the dimensionless vorticity within the tank during the half-sloshing periods were also included in **Figure 7**. Here, the vorticity term has been described as given in Equation (10). Where u, v, and w are the time-averaged velocity values in the x, y, and z directions, and ω_y is the vorticity in the plane perpendicular to the axis of "y". The vorticity term was normalised by the sphere diameter (D_p) and the undisturbed velocity (U_∞). It is worth noting that the undisturbed velocity is the depth-averaged velocity calculated for the passage of the wave crest from the centre of the tank without a sphere.

$$\omega_y = \frac{1}{2}\left(\frac{\partial u}{\partial z} - \frac{\partial w}{\partial x}\right) \tag{10}$$

5.2. Influence of Sloshing Modes on Boundary Layer Separation

Depending on the form of the obstacle, the pressure distribution caused by the velocity field controls the process of boundary layer separation when a solid body is in a steady flow[38]. However, for unsteady flows, boundary layer separation is also influenced by the net force due to the hydrostatic pressure distribution in the outer region far from the body, which is a function of the slope of the water surface. The flow conditions and geometry of the object are the determinants of these two factors. The influences of these hydrodynamic factors on boundary layer separation for the three modes described are discussed below.

According to **Figure 7**, in Mode 1, which is observed at the beginning of the sloshing half-cycle, the direction of the net force due to inertia (hydrostatic pressure gradient, i.e., Froude-Krylov Force) and the drag force are the same. The separation point (labelled "S" in **Figure 7**) is pushed downstream by the combined effects of inertia and drag. As a result, weaker lee-wake vortices are generated behind the spherical body. The appearance of the separation point of S is delayed, as shown schematically in **Figure 7(b1)**. Consequently, relatively weaker vortices are observed compared to Mode 2 and 3 in **Figure 7**.

In **Figure 7**, in Mode 2, the influence of net force due to hydrostatic pressure gradient (i.e., Froude-Krylov Force) on the sphere diminishes due to decreased water surface slope. The velocity around the sphere is higher compared to Mode 1. Despite this, the flow direction and net hydrostatic pressure force remain the same. It is a well-known phenomenon that under steady flow conditions, as velocity increases and turbulence develop, the separation point over the obstacle is shifted downstream due to momentum transfer, resulting in a reduction in vorticity. The numerical outputs showed that unexpectedly, the vortices become more pronounced in Mode 2, although the velocity around the body increases (**Figure 7**). This implies that for the pertinent hydraulic conditions examined in this study, the decreasing net hydrostatic pressure gradient is a more influential physical variable over the sphere compared to the velocity field in terms of generating vortices. In other words, enhancing velocity values around the sphere in Mode 2 cannot offset the influence of decreasing the water surface profile. However, it is worth highlighting that this finding is valid for the existing test conditions in this study. Different outcomes can be obtained for the different sloshing tank configurations and fluids.

During Mode 3, the flow direction remained unchanged and the same was observed with the examined half-sloshing duration. However, the direction of the Froude-Krylov force around the sphere and the inertial drag force are opposite. Additionally, the flow velocity around the spherical body declined significantly in Mode 3, as seen from the velocity profiles presented in **Figures 9** and **10**. Consequently, the downstream pushing impact of the flow on the separation point (i.e., S in **Figure 8**) diminishes. Furthermore, the pushing direction of net hydrostatic pressure on the separation point in the upstream direction. Hence, separation onset earlier, the wake region expands, and the strength of lee-wake vortices increases rear the sphere in Mode 3 (**Figure 8(a3–c3)**).

5.3. Comparison of Streamwise Velocity Fields Belonging to with and without Sphere Cases

Figures 8 and **9** show the variation of water surface level (WSL) and time-averaged streamwise velocity profiles obtained at different vertical sections during sloshing. These characteristic sections are half the diameter distance from the spherical body edges. The reason for choosing the half distance as a specific location is that these are the locations where the dimensionless vortices around the sphere are quite pronounced (**Figure 10**). As can be seen in **Figures 8** and **9**, the sloshing wave accelerates as it passes over the sphere. This acceleration, which was not observed in the no-sphere case, is due to the contraction effect in the vertical and horizontal planes around the body. **Figure 8(b1,b2)** show that as the sloshing wave approaches the spherical body, the computed velocity values on both sides of the sphere are greater than in the no-sphere scenario. Compared to the no-sphere case in **Figure 8(c2)**, although deceleration is observed in the wake zone of the sphere, acceleration is observed near the water surface above the sphere due to the contraction effect. The retardation of flow in the wake zone can be hypothesised to be induced by boundary layer separation and the development of recirculation around/behind the spherical body. This retardation of the flow observed at the rear of the body maintains its coherence during sloshing at a different strength. However, once the sloshing wave passes over the body during sloshing, the difference in WSLs for the no-sphere and sphere cases decreases, which is plausible.

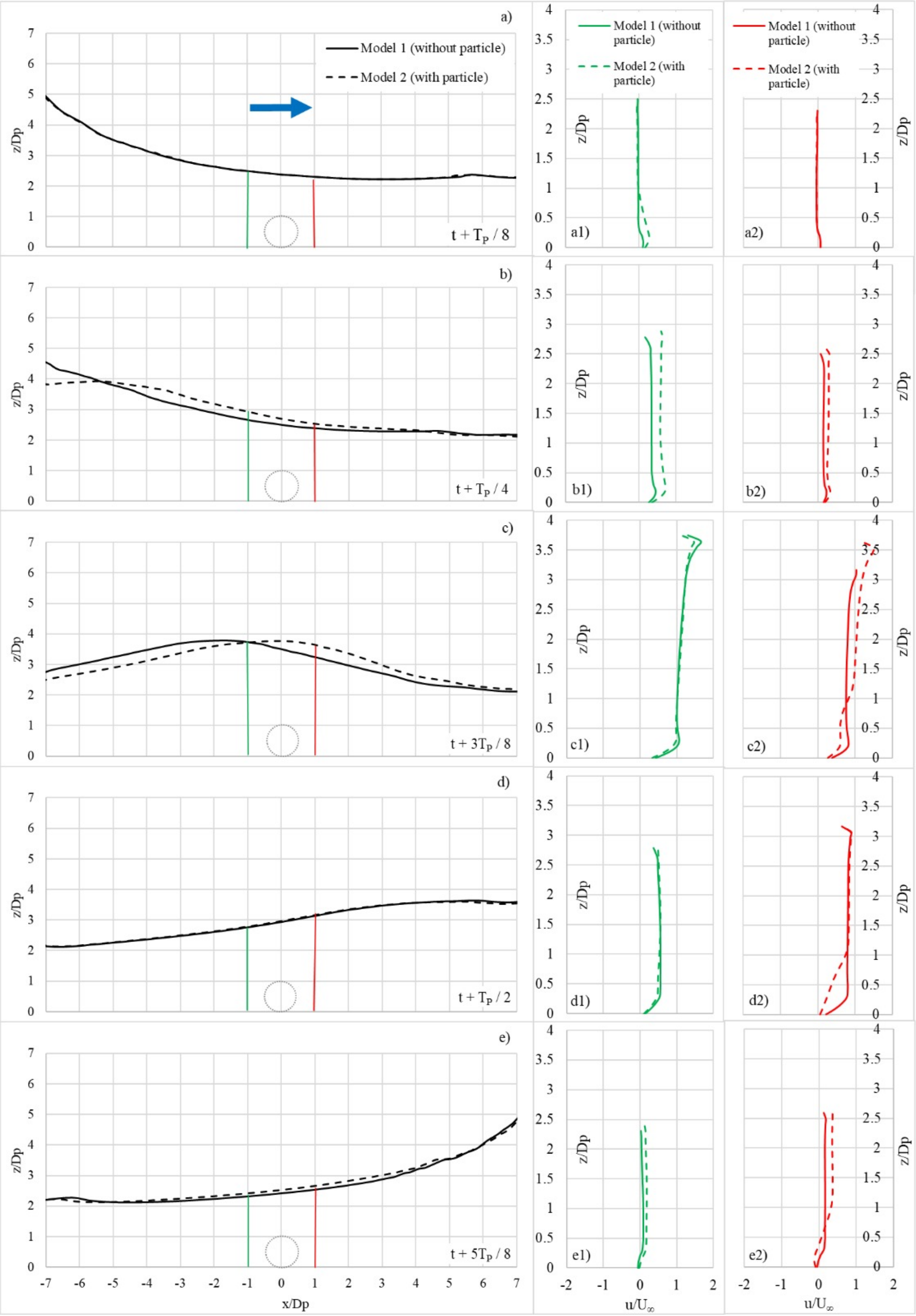

Figure 8. The variation of water surface level and instantaneous streamwise velocity profiles observed at characteristic vertical sections during half sloshing period. The motion is from left-to-right. The (**a–e**) shows the variation of WSL during half sloshing, (**a1–e1**) and (**a2–e2**) shows the variation of instantaneous velocity profile at green and red sections in (**a–e**).

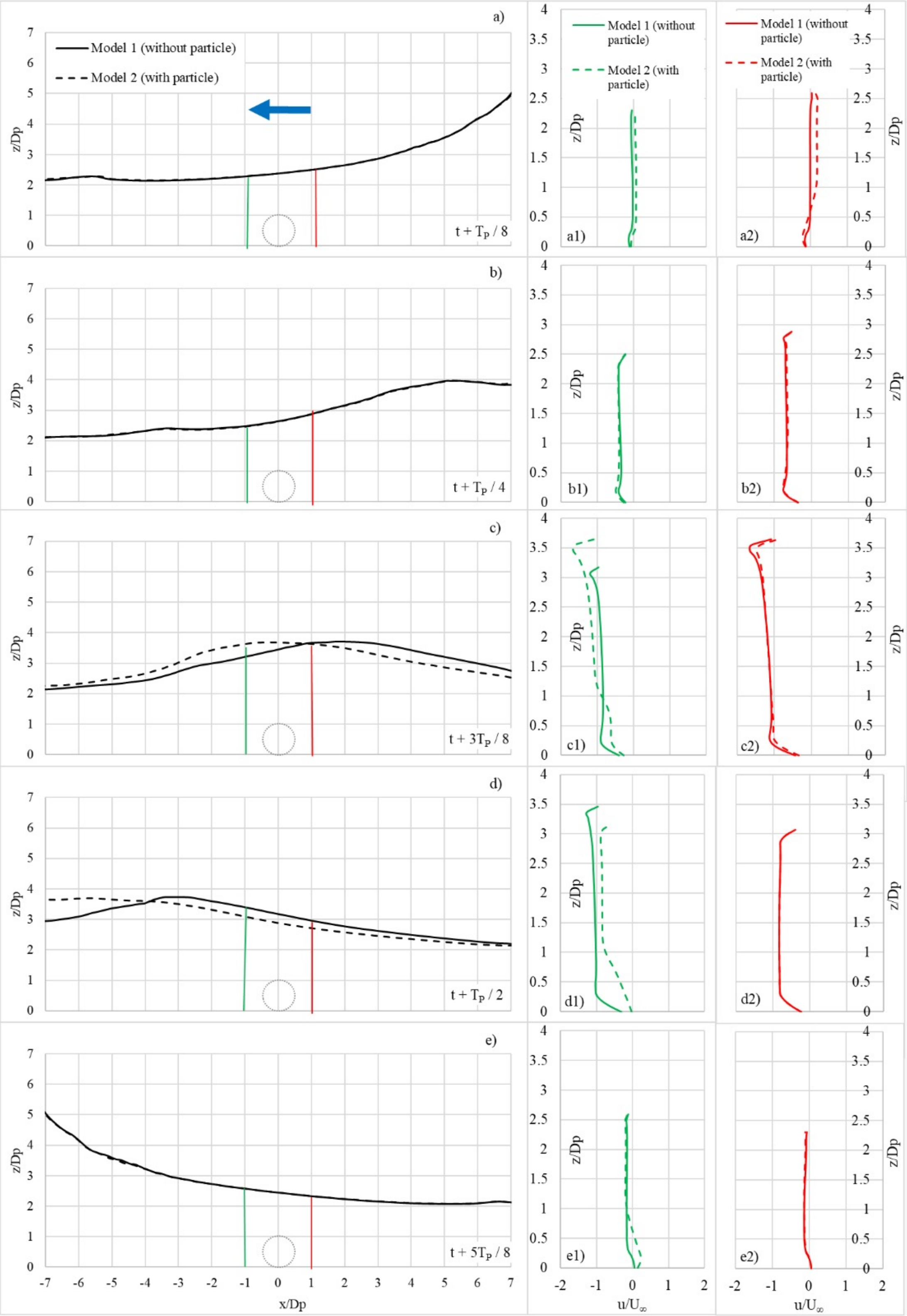

Figure 9. The variation of water surface level and streamwise velocity profiles observed at characteristic vertical sections during half sloshing period. The motion is from right-to-left. The (**a–e**) shows the variation of WSL during half sloshing, (**a1–e1**) and (**a2–e2**) shows the variation of instantaneous velocity profile at green and red sections in (**a–e**).

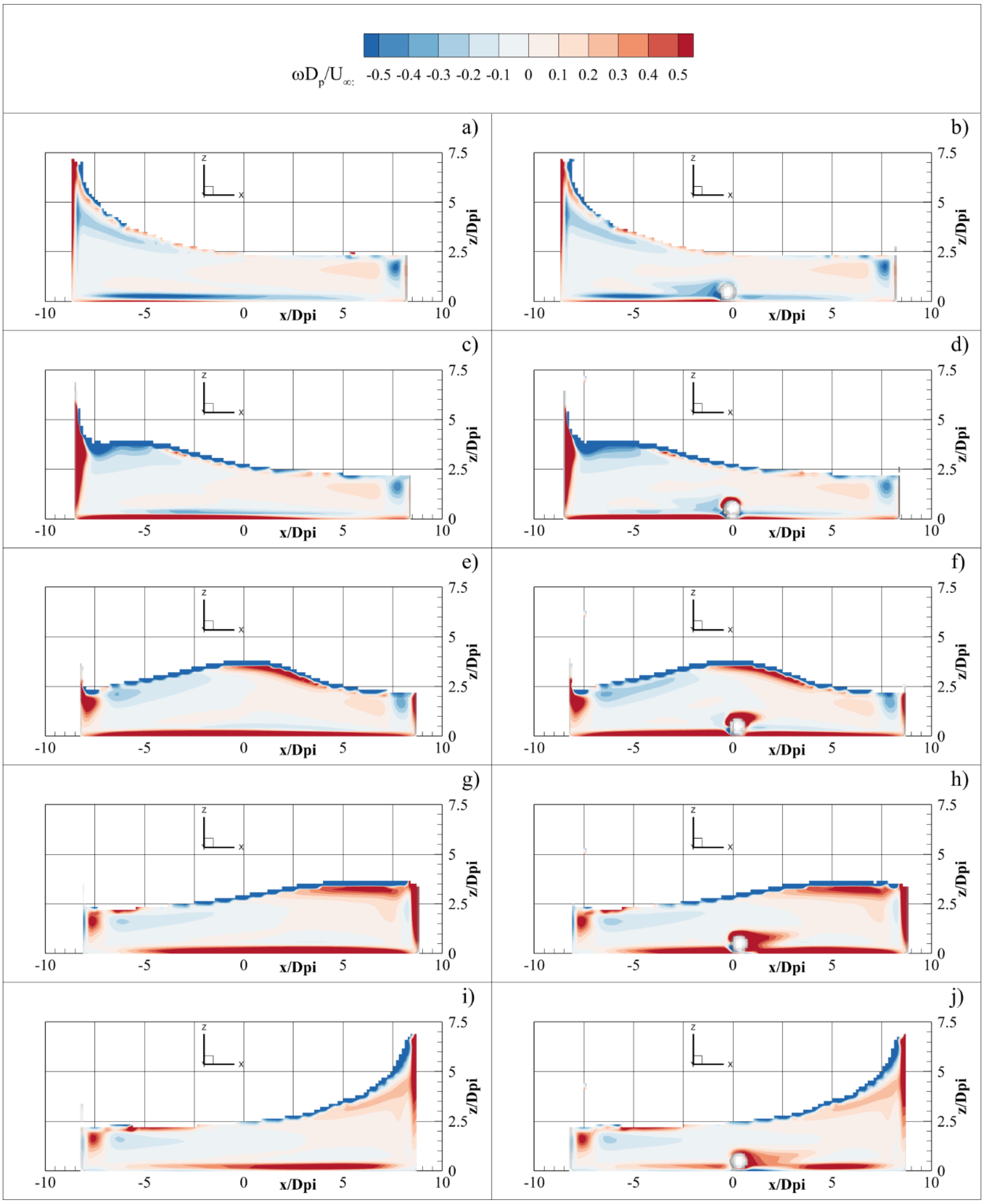

Figure 10. The variation of vorticity within the tank during half sloshing period in the form of contour-plots. The red color indicates counter-clockwise vorticity, the blue color indicates clockwise vorticity.

5.4. Comparison of Vorticity Fields Belonging to with and without Sphere Cases

Figure 10 shows the contour plots of the dimensionless vorticity inside the tank during a half-sloshing time. The friction-induced high vorticity fields are distinct near the bottom, sidewalls, and water surfaces for both cases (i.e., with and without spherical tanks). The common side of these regions is that they are in contact with the surrounding domain, i.e., bed or air.

Despite the highest velocity occurring during the passage of the wave peak over the sphere in Mode 2, the maximum vorticity in the wake of the sphere was not seen at that moment. Instead, the maximum vorticity was observed during the transition between Mode 2 and Mode 3, as shown in **Figure 10h**. At this moment (**Figure 10h**), while the net water mass transport is still from left to right, the direction of the net hydrostatic pressure-induced force is from right to left. The opposite directions of the net hydrostatic pressure gradient (Froude-Krylov force) and the current create the more pronounced boundary layer separation around the sphere, as conceptually illustrated and explained in **Figure 7c**. In other words, the inertial force (induced hydrostatic pressure gradient due to the steep water surface slope) amplifies the unfavourable pressure gradient, causing the separation of the boundary layer around the sphere. In addition, there is a time lag between the onset of maximum vorticity during half-sloshing and the occurrence of the wave peak over the sphere.

5.5. Hydrodynamic Analysis around the Sphere during a Half-Sloshing Cycle

The spatiotemporal variations of water surface levels, velocity fields, pressure gradient, and total force given in Equation 1 during the moment of the 3-major and 2-transition sloshing modes are shown in **Figure 11**. **Figure 11(a1–a5)** show the flow domain during the considered half-sloshing cycle, and **Figure 11c–g** show the temporal variations of the basic hydrodynamic variables on both sides (their locations are labelled 1 and 2 in **Figure 11b**) of the spherical object. The animated video from which the instantaneous cases in **Figure 11(a1–a5)** were extracted was also provided as supplemental material.

During the half-sloshing cycle period examined, the water surface elevation (**Figure 11d**) and pressure values have one maximum and two minimum values. Depending on the direction of the sloshing wave, a time lag was observed between the maximum and minimum pressure values at points 1 and 2. When examining the pressure fluctuations around the sphere during the sloshing half-cycle (**Figure 11(a1–a5)**), the pressure values were normalised by the ΔX values. The ΔX value is the distance from half the diameter to the sphere's edge (exact locations are shown as 1 and 2 in **Figure 11b**). The total length of ΔX is two diameters of the sphere. **Figure 11f** shows the temporal variation of the spatial pressure gradient (ΔP/dX) around the sphere. Two extrema were observed for spatial pressure gradient (ΔP/dX) during the half-sloshing cycle (**Figure 11f**). While the first and the highest positive values of ΔP/ΔX occurred between the moments of "transition a2-to-a3 in **Figure 11**", the lowest ΔP/ΔX emerged between the moments of " transition to aa3-to-a4".

In summary, the two most critical moments, in terms of generating the highest spatial pressure gradients, were detected just before and after Mode 2. However, these two cases share common characteristics. In a physical sense, just before Mode 2, the Froude-Krylov force, i.e. the inertial force, is at its highest because the slope of the water surface is at its steepest (in **Figure 11(a1–a5)**, the slope of the water surface is represented by the dashed line and denoted "dx"). In addition, the acceleration that affects the drag force on the sphere is greatest at this moment. This leads to the highest spatial pressure gradient occurring just before Mode 2. More precisely, just before Mode 2, the superposition of the high net hydrostatic pressure gradient (i.e. increased inertial forces) and the increased acceleration in the sloshing direction generates the highest spatial pressure gradient for that moment.

Likewise, just after Mode 2, the water surface slope is the steepest, but the net hydrostatic pressure gradient direction is opposite to the flow. As a result, the sign of the pressure gradient changed to negative due to the change in direction of the net hydrostatic pressure gradient. Thus, lower ΔP/ΔX values were observed just after Mode 2 compared to just before Mode 2. This changing sign of dP/dX clearly indicates that the influence of inertia forces prevails over the effect of drag force acting on the sphere. It is also worth highlighting that the spatial pressure fluctuation did not exhibit a monotonic pattern within a half-sloshing cycle, differing from the temporal variations of water level and the pressure monitored at points 1 and 2. This was probably due to the uncorrelated relationship between inertial and drag forces during a half-sloshing cycle.

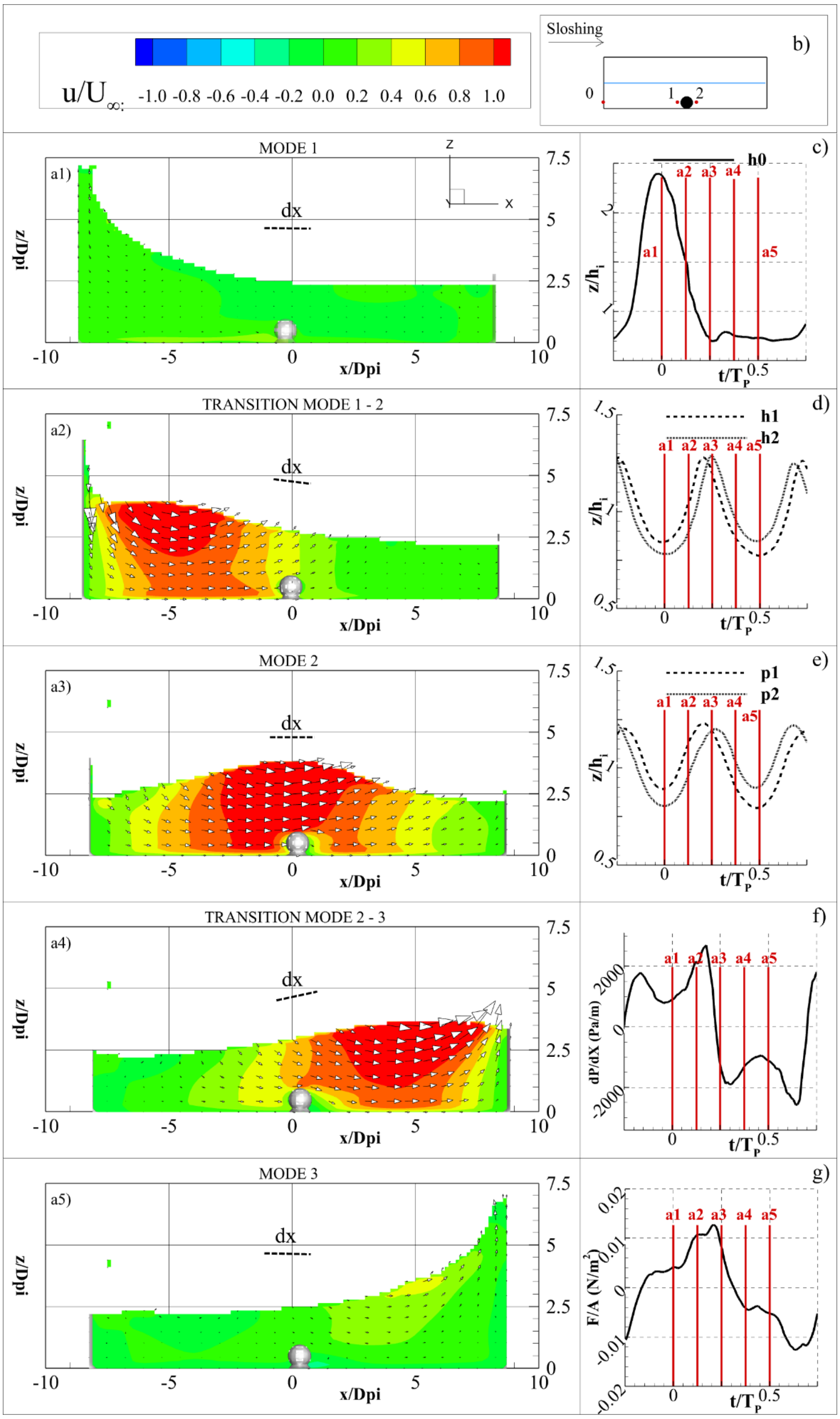

Figure 11. The spatiotemporal variations of water surface slopes, velocity vector fields, pressure gradient, and the drag force during 3-major and 2-transition sloshing modes. While contour-plots in (**a1–a5**) show the spatial distribution of the velocity field during 3 major and 2-transitional modes, the time series given in (**c–g**) presents the temporal variation of various physical variables. Time axis was normalized with the duration requires one sloshing cycle. Water surface elevations at the points of 0, 1, and 2 given in (**c**,**d**); the pressure values of P at the points of 1 and 2 are given in (**e**); the pressure difference between the points of 1 and 2 is given in (**f**); normalized drag force (drag force/projected area) acting on the spherical particle is given in (**g**). The red vertical sections appear in (**c–g**) corresponds to the moments of contour-plots given in (**a–a5**). The dashed line seen in (**a1–a5**) shows the water surface slopes between the points 1 and 2.

As explained above and seen in **Figure 11f**, ΔP/ΔX has the steepest temporal gradient $[(\mathrm{dP}/\mathrm{dX})/(\Delta t/\mathrm{T}_p)]$ between the moments of "transition mode 1-to-2 and Mode 2". If it is considered that the sphere and its area are constant, the steepest temporal pressure gradient $[(\mathrm{dP}/\mathrm{dX})/(\Delta t/\mathrm{T}_p)]$ points out that the force acting on the sphere is supposed to be the maximum at this moment. In fact, if we look at **Figure 11g**, we can see that the total force acting on the sphere reaches its maximum value during this period (the "Mode 1-to-2 and Mode 2 transition moments").

6. Discussion and Recommendation

The purpose of this study was to evaluate the kinematic and dynamic factors around a rigidly attached sphere located in the centre of the bottom of a sloshing tank. The numerical model was calibrated based on the conducted experiment with a constant sloshing period and unchanged still water depth. The main purpose of the actual test and simulation at constant duration and water depth was to verify the capabilities of the applied numerical model in a preliminary stage. Another study objective was to determine if the RANS model, known for its cost-effectiveness and fast computation time, provides physically plausible and consistent results. The model results demonstrated the applicability of a RANS model to model the flow field in the sloshing tank properly. However, it should be mentioned that depending on the period of sloshing, the influence of unsteadiness and hysteresis factors [4, 5, 11] modifies the values of pressure and forces acting on the sphere. To gain a deeper understanding of the kinematic and dynamic aspects associated with a spherical object in a sloshing tank, it is recommended that future studies focus on investigating the influence of the initial conditions in the tank, including water depth and size, as well as the amplitude of the excitation.

Furthermore, in addition to monitoring tank dynamics, it is proposed to study the effects of the generated flow motion on the bed surface particles using inertial sensors in a manner similar to that described in [39–41]. For the sake of simplicity, in this investigation, we have fixed the sphere in the centre of the bottom of the sloshing tank. As a result, the sphere's mobility was constrained throughout the simulations. The influence of the specific weight of the sphere on the observed data was thus completely ignored, and the sphere/particle motion was not investigated.

In addition, in this study, fluid properties (specific weight, temperature/viscosity) were kept constant throughout the experimental and numerical studies. However, fluid features greatly affect flow behaviour under the effect of external forces. For example, the fluid properties largely control the development of the boundary layer and the separation process around solid obstacles. Furthermore, several different fluids are used in sloshing tanks for different purposes in the industrial sector. Therefore, when adapting the results presented here, this consideration should be considered when attempting to generalise the results presented to such applications.

It should also be noted that this study explicitly excludes using a scaled hydraulic model. In accordance with the philosophy of Gravesen [42], the primary objective of the experiment was to gain a comprehensive understanding of the flow around a fixed sphere under the sloshing effect using non-intrusive, low-cost methods, namely a numerical model. The objective was to determine the nondimensional hydrodynamic variables governing the flow field around a sphere. Specifically, the effect of sloshing on boundary layer separation, the forces acting on a sphere, and the pressure gradient around the sphere were investigated.

The phenomenon of fluid flow around an object is a complex issue that is critical in many engineering contexts, as discussed above. The wake flow is expected to exhibit an increasing lack of stability and increased complexity for the high Reynolds number under the steady flow regime. Even under a steady flow condition, the flow around a bottom-mounted sphere can be even more complicated than the flow around a circular cylinder or sphere because of the no-slip effects caused by the wall and the lack of up-down symmetry. The high degree of unsteadiness of the bidirectional flow of the slosh motion further complicates the problem investigated in this study. Despite this extreme complexity, the examined problem in this study was investigated at a very basic level to constitute a suitable knowledge background for future studies. Hence, we only presented the results about the time-averaged variables, and we ignored the coherent flow structures. For future studies, we recommend investigating the generated coherent structures depending on the sloshing characteristics.

7. Conclusions

This study used a three-dimensional RANS-based numerical code to investigate the kinematic and dynamic variables in the vicinity of a single sphere rigidly attached to the bottom of a tank, which is exposed to sloshing motion. Experimental results were used to fine-tune the k-omega turbulence closure in the numerical model for a constant sloshing time. The following conclusions were drawn from the implemented model.

Three principal forms of motion (i.e., modes) were identified for a half-sloshing cycle around the sphere. The main motivation behind this category was to simplify hydrodynamic analysis. This categorisation was developed based on the magnitude and direction of the net inertial force due to the hydrostatic pressure gradient ($\Delta P/\Delta X$), where the conclusions pointed out that it is a highly influential variable on the hydrodynamic process around the sphere. Therefore, the modes were utilized in the spatiotemporal study of the kinematic and dynamic features surrounding the sphere. It is evident that the defined modes facilitate a more complete understanding of the separation process of the boundary layer surrounding the sphere and, consequently, of the drag force.

It was also seen that for the examined "sphere diameter-to-still water depth" ratio (17mm/50mm), the presence of the sphere at the bottom alters the propagation of sloshing motion in the tank. As a result, the wave passes over the sphere temporally earlier, and the maximum velocity deficit emerges during Mode 2 (i.e., the moment the sloshing wave passes over the sphere).

It was seen that maximum vorticity in the wake region of the sphere forms during Mode 3 (i.e., the net hydrostatic pressure gradient direction is opposite to flow for a given elevation in water). This situation revealed the significance of net hydrostatic pressure force around the sphere in separating the boundary layer. In other words, the net hydrostatic pressure force prevails over inertia's influence, dictating the separation process.

The findings showed that water surface level elevation and total pressure take one peak and two minima during a half-sloshing cycle. During the passage of the sloshing wave, time lags were observed in the pressure values observed at the half-diameter distance to the sphere edge. These temporal lags were significantly more apparent during the passage of sloshing waves over the spherical body than on the wave crest.

It was observed that the maximum spatial pressure gradient ($\Delta P/\Delta X$) occurred just before mode 2. At this moment, the slope of the water surface is the steepest, and the acceleration, which affects the total force acting on the sphere, is the highest. As a result, the calculated total force acting on the sphere also reaches its maximum value during this time interval.

Author Contributions

M.A.: Experimentation, Visualization, Investigation, Data curation, Formal analysis, Writing the original draft; O.Y.: Conceptualization, Investigation, Writing original Draft, Investigation, Formal Analysis; M.V.: Formal Analysis, Writing—Review & Editing; V.S.O.K.: Formal Analysis, Writing—Review & Editing. All authors have read and agreed to the published version of the manuscript.

Funding

This research received no external funding.

Data Availability Statement

The data is open to other researchers and can be provided upon request from the authors of the present study.

Acknowledgements

The authors present their appreciation to Alanya Alaaddin Keykubat University for allowing the utilisa-

tion of hydraulic facilities in the laboratory.

Conflict of Interest

The authors disclosed no conflict of interest. All the co-authors have seen and agree with the contents of the manuscript, and there is no financial interest to report.

References

[1] Brizzolara S, Savio L, Viviani M, Chen Y, Temarel P, Couty N, Hoflack S, Diebold L, Moirod N, Iglesias A (2011) Comparison of experimental and numerical sloshing loads in partially filled tanks. Ships Offshore Struct, 6(1–2):15–43. DOI: https://doi.org/10.1080/17445302.2010.522372

[2] Disimile P, Toy N (2019) The imaging of fluid sloshing within a closed tank undergoing oscillations. Results Eng 2:100014. DOI: https://doi.org/10.1016/j.rineng.2019.100014

[3] Gurusamy S, Sanapala V, Kumar D, Patnaik B (2021) Sloshing dynamics of shallow water tanks: Modal characteristics of hydraulic jumps. J Fluids Struct 104:103322. DOI: https://doi.org/10.1016/j.jfluidstructs.2021.103322

[4] Gargari MK, Kirca VSO, Yagci O (2021) Experimental investigation of gradually varied unsteady flow passed a circular pile. Coast Eng 168:103926. DOI: https://doi.org/10.1016/j.coastaleng.2021.103926

[5] Erdog E, Yagci O, Kirca, VSO (2022) Hysterical effects in flow structure behind a finite array of cylinders under gradually varying unsteady flow conditions. J Ocean Eng Mar Energy 8(3):247–267. DOI: https://doi.org/10.1007/s40722-022-00229-y

[6] Odar F, Hamilton WS (1964) Forces on a sphere accelerating in a viscous fluid. J Fluid Mech 18(02):302. DOI: https://doi.org/10.1017/s0022112064000210

[7] Anderson TJ, Uhlherr PHT (1977) The influence of stream turbulence on the drag of freely entrained spheres. In Proceedings of the 6th Australasian Hydraulics and Fluid Mechanics Conference, Adelaide, SA, Australia

[8] Mei R (1994) Flow due to an oscillating sphere and an expression for unsteady drag on the sphere at finite Reynolds number. J Fluid Mech 270:133–174. DOI: https://doi.org/10.1017/s0022112094004222

[9] Chang EJ, Maxey MR (1994) Unsteady flow about a sphere at low to moderate Reynolds number. Part 1. Oscillatory motion. J Fluid Mech 277:347–379. DOI: https://doi.org/10.1017/s002211209400279x

[10] Alassar R, Badr H (1997) Oscillating viscous flow over a sphere. Comput Fluids 26(7):661–682. DOI: https://doi.org/10.1016/s0045-7930(97)00017-0

[11] Song T, Graf WH (1996) Velocity and Turbulence Distribution in Unsteady Open-Channel Flows. J Hydraul Eng 122(3):141–154. DOI: https://doi.org/10.1061/(asce)0733-9429(1996)122:3(141)

[12] Brucato A, Grisafi F, Montante G (1998) Particle drag coefficients in turbulent fluids. Chem Eng Sci 53(18):3295–3314. DOI: https://doi.org/10.1016/s0009-2509(98)00114-6

[13] Luo K, Wang Z, Fan J (2010) Response of force behaviors of a spherical particle to an oscillating flow. Phys lett A 374(30):3046–3052. DOI: https://doi.org/10.1016/j.physleta.2010.05.036

[14] Valyrakis M, Diplas P, Dancey CL, Greer K, Celik AO (2010) Role of instantaneous force magnitude and duration on particle entrainment. J Geophys Res Earth Surf 115(F2). DOI: https://doi.org/10.1029/2008jf001247

[15] Celik AO, Diplas P, Dancey CL, Valyrakis M (2010) Impulse and particle dislodgement under turbulent flow conditions. Phys Fluids 22(4):046601. DOI: https://doi.org/10.1063/1.3385433

[16] Valyrakis M, Diplas P, Dancey CL (2011) Prediction of coarse particle movement with adaptive neuro-fuzzy inference systems, Hydrol Proc, 25(22):3513–3524. DOI: https://doi.org/10.1002/hyp.8228

[17] Ibrahim RA, Pilipchuk VN, Ikeda T (2001) Recent advances in liquid sloshing dynamics. Appl Mech Rev 54(2):133–199 DOI: https://doi.org/10.1115/1.3097293

[18] Bakic V (2003) Experimental investigation of turbulent flows around a sphere. PhD Thesis, 83pp, University of Technical University of Hamburg.

[19] Sadikin A, Yunus NaM, Abdullah MK, Mohammed AN (2014). Numerical Study of Flow Past a Solid Sphere at Moderate Reynolds Number. Applied Mechanics and Materials, 660, 674–678. DOI: https://doi.org/10.4028/www.scientific.net/amm.660.674

[20] Sumer BM, Fredsøe J (2006) Hydrodynamics around cylindrical structures, vol 26. World Scientific, Singapore DOI: https://doi.org/10.1142/3316

[21] Cao Y, Tamura T (2020). Large-eddy simulation study of Reynolds number effects on the flow around a wall-mounted hemisphere in a boundary layer. Physics of Fluids, 32(2). DOI: https://doi.org/10.1063/1.5142371

[22] Achenbach E (1968) Distribution of local pressure and skin friction around a circular cylinder in cross-flow up to Re = 5×10^6. Jour-

nal of Fluid Mechanics, 34(4), 625–639. DOI: https://doi.org/10.1017/s0022112068002120

[23] Constantinescu G, Squires K (2003) LES and DES Investigations of Turbulent Flow over a Sphere at Re=10,000. Flow, Turbulence and Combustion 70, 267–298. DOI: https://doi.org/10.1023/B:APPL.0000004937.34078.71

[24] Atmani R, Brima A, Askovic R (2009). Study of Three-Dimensional Separation of Boundary Layer Over Blunt Bodies. Journal of Hydrodynamics/Journal of Hydrodynamics. Ser. B, 21(1), 100–107. DOI: https://doi.org/10.1016/s1001-6058(08)60124-9

[25] Munson BR, Okiishi TH, Huebsch WW, Rothmayer AP (2013). Fundamentals of fluid mechanics. John Wiley & Sons, Inc., pp, 796.

[26] O, Yildirim I, Celik MF, Kitsikoudis V, Duran Z, Kirca VSO (2017) Clear water scour around a finite array of cylinders. Appl Ocean Res 68. 114–129. DOI: https://doi.org/10.1016/j.apor.2017.08.014

[27] Yagci O, Karabay Ö, Strom K (2021). Bleed flow structure in the wake region of finite array of cylinders acting as an alternative supporting structure for foundation. Journal of Ocean Engineering and Marine Energy, 7(4), 379–403. DOI: https://doi.org/10.1007/s40722-021-00208-9

[28] Aksel M, Yagci O, Kirca VSO, Erdog E, Heidari N (2021) A comparative analysis of coherent structures around a pile over rigid-bed and scoured-bottom. Ocean Eng. DOI: https://doi.org/10.1016/j.oceaneng.2021.108759

[29] Bayon A, Valero D, García-Bartual R, Vallés-Morán FJ, López-Jiménez PA (2016) Performance assessment of OpenFOAM and FLOW-3D in the numerical modeling of a low Reynolds number hydraulic jump. Environ Model Softw 80:322–335. DOI: https://doi.org/10.1016/j.envsoft.2016.02.018

[30] Chen SC, Tfwala SS (2018) Performance assessment of FLOW-3D and X flow in the numerical modelling of fish-bone type fishway hydraulics, 7th IAHR International Symposium on Hydraulic Structures, Aachen-Germany, pp 272-282. DOI: https://doi.org/10.15142/T3HH1J

[31] Ghasemi M, Soltani-Gerdefaramarzi S (2017) The Scour Bridge Simulation around a Cylindrical Pier Using Flow-3D. J Hydrosci Environ 1(2):46-54. DOI: https://doi.org/10.22111/JHE.2017.3357

[32] M, Maliki AY, Ahmad M, Sani WN, Yaakob O, Samo K (2017) Numerical Simulation of Wave Flow Over the Overtopping Breakwater for Energy Conversion (OBREC) Device. Procedia Eng, 194:166–173. DOI: https://doi.org/10.1016/j.proeng.2017.08.131

[33] Najafi-Jilani A, Niri MZ, Naderi N (2014) Simulating three-dimensional wave run-up over breakwaters covered by antifer units. International Journal of Naval Architecture and Ocean Engineering, 6(2):297–306. DOI: https://doi.org/10.2478/ijnaoe-2013-0180

[34] Richardson JE, Panchang V (1998) Three-Dimensional Simulation of Scour-Inducing Flow at Bridge Piers. J Hydraul Eng, 124(5):530-540. DOI: https://doi.org/10.1061/(ASCE)0733-9429(1998)124:5(530)

[35] Smith HD, Foster DL (2005) Modelling of Flow Around a Cylinder Over a Scoured Bed. J Waterw Port Coast Ocean Eng, 131(1):14–24. DOI: https://doi.org/10.1061/(ASCE)0733-950X(2005)131:1(14)

[36] Ma C, Oka M (2020) Numerical Investigation on Sloshing Pressure for Moss-Type LNG Tank Based on Different SPH Models. In The 30th International Ocean and Polar Engineering Conference. OnePetro.

[37] SR, Hansen EW (2006) Numerical simulations of sloshing in rectangular tanks. In: International Conference on Offshore Mechanics and Arctic Engineering, vol. 47497, pp 675-682 DOI: https://doi.org/10.1115/OMAE2006-92248

[38] Schlichting H, Gersten K (2000) Boundary-Layer Theory 8th ed. Springer.

[39] AlObaidi K, Xu Y, Valyrakis M. (2020) The Design and Calibration of Instrumented Particles for Assessing Water Infrastructure Hazards, J Sensor and Actuator Net, 2020, 9(3):36(1–18). DOI: https:/doi.org/10.3390/jsan9030036

[40] AlObaidi K, Valyrakis M (2021a) A sensory instrumented particle for environmental monitoring applications: development and calibration, IEEE Sensors, 21(8):10153–10166. DOI: https:/doi.org/10.1109/JSEN.2021.3056041

[41] AlObaidi K, Valyrakis M (2021b) Linking the explicit probability of entrainment of instrumented particles to flow hydrodynamics, Earth Surface Processes and Landforms, 46(12):2448–2465. DOI: http://doi.org/10.1002/esp.5188

[42] Gravesen H (2003) The importance of experiments for marine engineering design practice. Hydrolab II: towards a balanced methodology in European hydraulic research, Budapest, May 22–23.